V International Conference on Computational Methods for Coupled Problems in Science and Engineering
COUPLED PROBLEMS 2013
S. Idelsohn, M. Papadrakakis and B. Schrefler (Eds)

NUMERICAL INVESTIGATION OF CONTINUOUS FIBER GLASS DRAWING

Q. CHOUFFART*, P. SIMON† AND V. E. TERRAPON*

*Department of Aerospace and Mechanical Engineering
University of Liege
1 Chemin des chevreuils, 4000 Liège, Belgium
e-mail: vincent.terrapon@ulg.ac.be - web page: http://www.mtfc.ulg.ac.be/

†3B - The Fibreglass Company
Rue de Charneux 59, 4651 Battice, Belgium
e-mail: philippe.simon@3b-fibreglass.com - web page: http://www.3b-fibreglass.com

Key words: Fiberglass drawing, glass forming, fiberization, multiphysics simulation

Abstract. The physics of glass fiber drawing is studied through numerical simulations and experimental measurements, with a focus on the fluid region, from the hole tip at the bushing plate to the glass transition point. The influence of the different heat transfer mechanisms is investigated to understand their respective impact on fiberization, such as fiber radius attenuation and internal stresses. Numerical predictions are then compared to experimental data measurements obtained from a dedicated fiberization unit. Numerical and experimental results show a good agreement. In particular, it is found that the ambient air temperature and the radiation have an important impact on the fiber cooling rate. Moreover, for a prescribed fiber diameter, internal stresses are lower when operating at a higher temperature.

1 Introduction

Due to their good mechanical properties, glass fibers are frequently used for the reinforcement of composite materials in many engineering fields. The industrial process to manufacture these fibers consists in continuously drawing and cooling a glass melt into fibers. The liquid glass, which is melted upstream in a furnace, flows through a bushing plate, thus forming long filaments. The bushing plate is typically composed of 1'000 to 8'000 holes, each with a diameter of about 1 to 2 mm. The different holes have a cylindrical protuberance on the lower side of the bushing plate, which is hereafter simply referred to as "tip". These filaments are then quickly cooled by fins and water sprays to reach glass transition, and undergo solidification before being wound at high velocity (see figure 1). During this process, the fiber diameter is strongly attenuated (by up to

two orders of magnitude). The final fiber diameter (typically 10 to 34 μm) is controlled by the drawing velocity and the glass flow rate. It has been observed during industrial production that this continuous process is highly sensitive to small disturbances that can lead to fiber breaking. The fiber breaking problem, common across the glass fiber industry, strongly limits the efficiency of the process. In particular, the break of a single fiber requires taking the specific bushing position off-line during several minutes, and leads to a large quantity of glass waste, which can typically amount to up to 10% of the total glass production. Therefore, the overall objective of the present research is to understand the physical mechanisms underlying fiber breaking and to identify a strategy to reduce it. In this context, the first step is to characterize the physics governing the glass fiber forming through numerical modeling of a single fiber.

Different studies have already been performed on the physics of fiber glass drawing, but unfortunately many of the results still remain confidential within industrial companies. During the 1960's, Glicksman [1] used a one-dimensional Newtonian fluid model to understand the behavior of the fiber during the manufacturing process. Neglecting two-dimensional effects was justified by the very small slope of the free surface in the central region, i.e. far away from the tip. His theorical study was compared to experimental data and good agreement was found, thus validating the one-dimensional assumption for the central region. However, this simplification is not adequate to accurately represent the region very close to the tip. Huynh and Tanner [2] solved numerically the two dimensional problem using a finite elements method. They showed that radiation is the dominant mode of cooling in the vicinity of the tip exit and they proposed to use a non-constant effective emissivity in order to take into account the radius attenuation along the axial component. Purnode [3, 4] also used a two-dimensional finite elements model and relied on both steady and unsteady simulations. His results confirmed that radiation is the main heat transfer mechanism near the tip exit, while convection becomes dominant further away. Moreover, surface tension was shown to be destabilizing while convection had a stabilizing effect. Von der Ohe [5] performed a numerical parametric study for different glass types and operating windows. She pointed out that the drawing speed and cooling conditions of the surrounding air are important, in particular for the final product properties. On the other hand, the experimental study by Rekhson [6] on a bushing plate with about hundred holes indicates that fiber break is mostly due to inhomogeneous heat patterns on the bushing plate. More recently, Liu [7] investigated numerically the variations of the final fiber diameter due to variabilities in the process and identified the ambient air and furnace temperatures as their main cause. These findings led to the development of a control system to reduce the variation of the fiber diameter due to both these effects by adjusting the winder velocity.

Although these models led to relative good agreement with experimental measurements, their accuracy could still be improved. In particular, internal radiation is often neglected and constant emissivity is typically assumed along the fiber surface. Additionally, the environment around the fiber is generally considered as isothermal although

experimental measurements demonstrate that it is not the case. These simple models are extended here to account for variations in the surface emissivity for radiative, and variations in the ambient air temperature for convective heat losses. A sensitivity analysis on some key parameters is performed and numerical predictions are compared to experimental data from the literature and from measurements performed on a dedicated fiberization unit.

2 Problem statement and governing equations

Glass fiber drawing involves various complex physics. It is generally accepted that a forming fiber can be divided into three regions as shown in figure 1. The first region is the forming shape at the tip exit where the largest radius attenuation occurs. As the temperature is high, the viscous glass melt flows as a free-surface jet and the heat transfers are essentially dominated by radiation. The typical length of this region is a few millimeters from the tip exit. The "draw-down region" then starts where the slope of the free surface becomes very small and ends at glass transition. In this region, the viscosity increases dramatically until the glass fully solidifies. Its length is typically about a few centimeters, and convection is the main cooling mechanism as a large heat exchange is promoted by the high drawing velocity. Finally, the last region is defined as the region after the transition where the material is in a glassy state. The fiber motion is there that of a solid rod translating axially. Note that the defining characteristics of these three regions change smoothly and continuously, so that their boundaries are only qualitative.

This work focuses on the first two regions. The model used is based on following assumptions: the glass material is modeled as an incompressible Newtonian viscous fluid, the flow is assumed to be axisymmetric, and only the steady state is considered. The liquid glass can be described by the basic governing equations of mass, momentum and energy conservation:

$$\boldsymbol{\nabla} \cdot \mathbf{v} = 0, \tag{1}$$

$$\rho \left(\mathbf{v} \cdot \boldsymbol{\nabla} \right) \mathbf{v} = \boldsymbol{\nabla} \cdot \boldsymbol{\sigma}, \tag{2}$$

$$\rho c_p \mathbf{v} \cdot \boldsymbol{\nabla} T = \boldsymbol{\sigma} : \boldsymbol{\nabla} \mathbf{v} + \boldsymbol{\nabla} \cdot (k \boldsymbol{\nabla} T) - \boldsymbol{\nabla} \cdot \dot{\mathbf{q}}_r, \tag{3}$$

where $\mathbf{v}$ is the velocity vector, T the temperature, $\boldsymbol{\sigma}$ the stress tensor, and $\dot{\mathbf{q}}_r$ the radiative heat flux. The density ρ, the specific heat c_p and the conductivity k are considered constant as their temperature dependence is low in the temperature range considered. For a Newtonian fluid the stress tensor is equal to $\boldsymbol{\sigma} = -p\mathbf{I} + 2\eta \boldsymbol{D}$, where p is the isotropic pressure and $\boldsymbol{D} = 1/2(\boldsymbol{\nabla}\mathbf{v} + \boldsymbol{\nabla}\mathbf{v}^T)$ the strain-rate tensor. The dependence of the viscosity η on the temperature T is given by Fulcher's law

$$\eta = 10^{-A + \frac{B}{T - T_0}}, \tag{4}$$

where A, B and T_0 are three constants that depend on the material considered. Note that the velocity and stress fields only depend on the temperature through the viscosity.

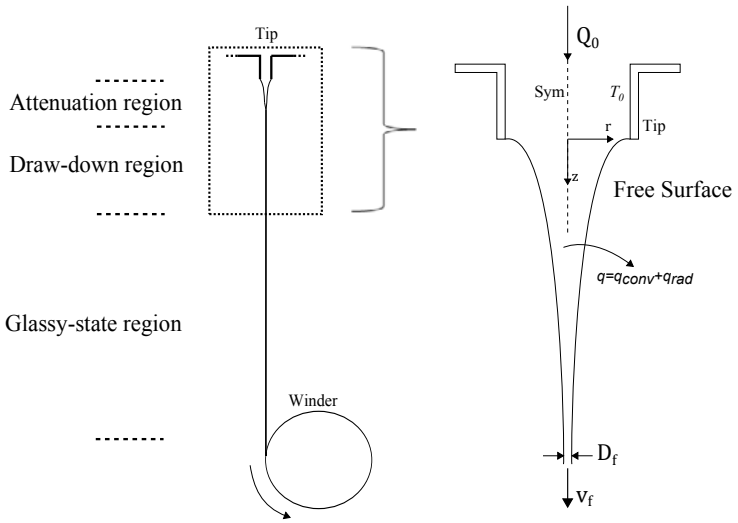

Figure 1: Schematics of the drawing process for a single fiber, computational domain (indicated by the dotted frame on the left) and boundary conditions.

2.1 Boundary conditions

The geometry is composed of the tip and the fiber. The problem being axisymmetric, only a slice is included in the computational domain. At the tip inlet, the volumetric flow rate is imposed based on the height H of the glass column and the viscosity of the melt [8]:

$$Q_0 = \frac{\pi}{8\eta}\left(-\frac{\partial p}{\partial z}\right) R_0^4 = \frac{\pi}{8\eta}\left(\frac{\rho g H}{h}\right) R_0^4, \tag{5}$$

where g is the gravity constant and R_0 and h are the tip radius and length, respectively. It is well-accepted that the viscosity at the tip should be around 1000 Poise to ensure fiberization, which corresponds to a temperature called T_3 (3 for $\log_{10}\eta = 3$). As a result, a temperature T_0 around the value of T_3 (generally between $\log_{10}\eta = 2.5$ and $\log_{10}\eta = 3$) is used as boundary condition for the tip walls, where a no-slip condition is imposed for the velocity field. At the outlet, a constant drawing velocity v_f is imposed in the axial direction. The final fiber diameter is thus directly controlled by the inlet volumetric flow rate and the drawing velocity.

Along the free surface, the interface condition is given by

$$\mathbf{n}\cdot\boldsymbol{\sigma}_g - \mathbf{n}\cdot\boldsymbol{\sigma}_a = \gamma\mathbf{n}\cdot(\boldsymbol{\nabla}\cdot\mathbf{n}), \tag{6}$$

$$\mathbf{v}\cdot\mathbf{n} = 0, \tag{7}$$

where γ is the surface tension assumed constant, $\boldsymbol{\sigma}_g$ and $\boldsymbol{\sigma}_a$ the interface stress for glass and air, respectively, and $\mathbf{n}$ the surface normal. Note that $\boldsymbol{\sigma}_a$ is neglected here.

Both convective and radiative heat losses take place at the free surface. The heat flux leaving the fiber can thus be written as

$$\dot{q}_s = \dot{q}_{conv} + \dot{q}_{rad} = h_c \left(T_s - T_{ext}\right) + \epsilon\sigma \left(T_s^4 - T_{ext}^4\right), \tag{8}$$

where h_c is the convective heat transfer coefficient, T_s the surface temperature, T_{ext} the ambient temperature around the fiber, ϵ the emissivity of the fiber surface and σ the Stefan-Boltzmann constant.

The convective cooling is induced by the high drawing velocity of the fiber (of the order of 20 m/s) that entrains ambient air. Many previous studies have considered a constant ambient air temperature. However, experimental measurements show a strong gradient of T_{ext} along the fiber. This is due to the heating of the air in the vicinity of the bushing plate (whose temperature is around T_3) and its entrainment downwards by the fiber. In the present model, the variations of the ambient temperature T_{ext} along the vertical coordinate z are considered by fitting experimental measurements of T_{ext}. The convective heat transfer coefficient h_c is approximated by Kase and Matsuo correlation for a thin cylinder moving axially [9]

$$h_c = 0.42 \frac{k_a}{D} \mathrm{Re}^{0.334}, \tag{9}$$

where k_a is the air conductivity and $D(z)$ the fiber diameter, and the Reynolds number is defined as $\mathrm{Re} = v_z D/\nu_a$, with ν_a and v_z the air kinematic viscosity and the fiber axial velocity at the surface, respectively. This relation has been used in many previous studies and seems to be adequate [3, 5, 6]. Note also that the dependence of the air properties (e.g., k_a, ν_a) on the temperature T_{ext} is included, and dry air is assumed.

The glass melt is a semi-transparent medium for some range of wavelengths and, thus, contributes in addition to conduction to internal heat transfers. Consequently, an accurate radiation model would be required to obtain the precise internal temperature profile and surface radiative flux. In order to simplify the model and reduce CPU time, internal radiation is modeled here through an effective emissivity $\epsilon = \epsilon(D, T)$ that takes into account the variations of the fiber diameter D and surface temperature T_s. At the same time, the radiative internal heat flux $\dot{\mathbf{q}}_r$ in Eq. (3) is neglected. The emissivity ϵ decreases with decreasing D and increasing T. Consequently, the change in emissivity along the fiber corresponds to a balance between these two effects. The effective emissivity is approximated by a cubic and linear fit of experimental measurements for D and T, respectively.

The governing equations are solved numerically with ANSYS POLYFLOW [10] using a finite-element computational fluid dynamic method. The free surface is treated with an Arbitrary Lagrangian-Eulerian (ALE) formulation.

3 Experimental approach

A dedicated fiberization unit has been developed to study experimentally the drawing of a single fiber. Figure 2 shows the overall apparatus. Glass cullets are melted at a

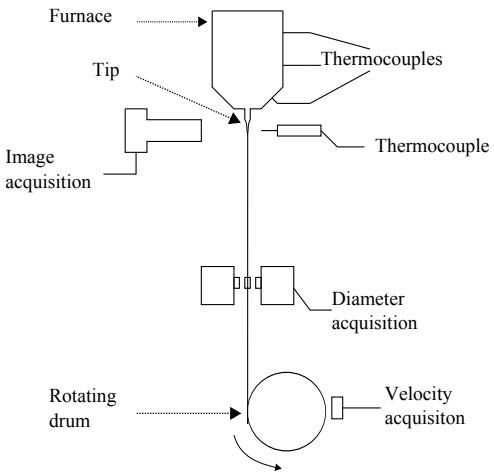

Figure 2: Schematics of the experimental fiberization unit and measurement devices.

temperature of up to 1450°C inside an electrically heated platinium-rhodium container. The temperature inside the furnace is monitored through three thermocouples located at different heights. The furnace temperature is continuously maintained at a constant temperature based on measurements from the middle thermocouple. The forming fiber is drawn from one single cylindrical tip by a rotating drum. The fiber diameter can be measured on-line through a laser diffractometer, from off-line optical measurements of fiber samples, or from measuring off-line the total mass of fiber produced. The take-up velocity of the rotating drum is also measured on-line. A camera with a macro lenses is used to take high-resolution digital photographs of the fiber meniscus, which are then post-processed to obtain the fiber diameter. Finally, the temperature of the ambient air around the fiber is measured through a thermocouple at different axial locations z. Measurement uncertainties on the velocity and final fiber diameter are of the order of 0.2% and 1 μm, respectively.

4 Results and discussion

4.1 Validation

The numerical predictions are first validated through comparisons with experimental studies from the literature and from measurements obtained on the dedicated fiberization unit described above. In particular, the experimental data from Glicksman's case M5 [1] are used. We focus here on the meniscus attenuation, as it represents the easiest macroscopic quantity to measure experimentally, and is often the only one available in the literature. Additionally, the variation of the fiber diameter is also a good proxy for the velocity gradients. For the second set of experimental data, the fiber diameter is obtained from high-resolution photographs of the fiber free-surface. Note that only the upper part of the cone shape is measured in this case. The respective process conditions are summarized in table 1 and results are shown in figure 3(a). A good agreement can

be observed for both cases, especially in the upper part of the cone shape. Nonetheless, some discrepancies can be seen for the lower part (Glicksman's case). This could be due to larger relative errors in the measurements as the fiber radius becomes very small in this region. At such a small radius, the fiber is represented by only a few pixels on the photograph so that the identification of the free-surface becomes much less accurate. Furthermore, the uncertainties of glass properties can provide error on simulation results.

Table 1: Experimental conditions for the two validation cases: volumetric flow rate Q_0, tip diameter D_0, tip temperature T_0, and drawing velocity v_f.

	Q_0 [m^3/s]	D_0 [mm]	T_0 [°C]	v_f [m/s]
1) Glicksman's M5 case [1]	$3.171 \cdot 10^{-9}$	1.72	1227	25.88
2) Present experiment	$4.720 \cdot 10^{-10}$	1.20	1308	1.55

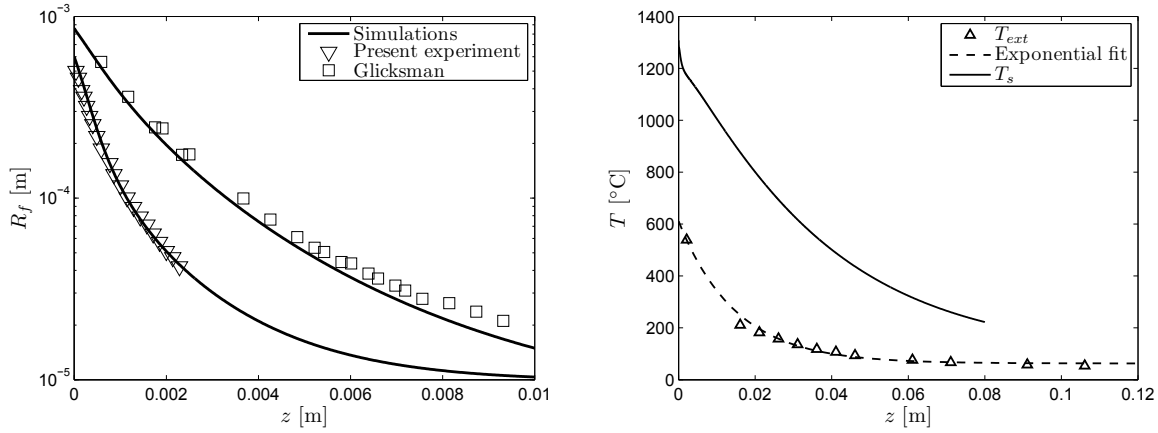

(a) (b)

Figure 3: (a) Comparison between the predicted and measured fiber radius $R(z)$ as a function of the distance z from the tip for the two experiments of table 1. (b) Computed surface temperature T_s and measured air temperature T_{ext} as a function of z for experiment 2. The dotted line represents an exponential fit of the measured T_{ext}.

4.2 Heat transfer analysis

Heat transfers play a critical role in the process, as the glass material is quickly cooled from the melt temperature to ambient temperature. Moreover, the thermal history, and in particular the cooling rate, determine the microscopic structure of the glassy state, and thereby, the properties of the solid glass. As such, the process and the fiber properties

are very sensitive to variations in the environment. For instance, it has been frequently observed that changes in the environment properties can lead to a large increase of the fiber breaking rate.

Unless otherwise stated, the following results are based on the second experiment of table 1 with an effective emissivity $\epsilon(D,T)$ and a variable external temperature T_{ext}. Figure 3(b) shows the temperature T_s along the fiber surface as a function of the distance from the tip, illustrating the rapid cooling over a short distance. In the same figure, the measured external temperature T_{ext} demonstrates that the assumption of a constant T_{ext} is not adequate, as this temperature varies from about 650°C at the tip to room temperature further away. The normalized temperature profile $\Delta T(r,z) \equiv T(r,z) - T_s(z)$ at different z locations is shown in figure 4(a). One can observe that the maximum temperature difference across a fiber section first increases to reach a maximum value of about 8°C at a distance $z \approx 2.5$ mm, and then slowly decreases to become much lower than 1°C. However, the fiber radius $R(z)$ experiences simultaneously a strong attenuation, so that the radial temperature gradients increase continuously.

The relative contributions of the radiative flux $\dot{q}_{rad}$ and convective flux $\dot{q}_{conv}$ to the total heat flux $\dot{q}_s$ at the fiber surface are shown in figure 4(b). These results confirm that radiation dominates in the first region of the forming fiber very close to the tip. Convection then becomes the major mechanism for heat loss when the fiber radius approaches its final value. The total heat flux shows two maxima corresponding to the maximum radiative and convective heat fluxes, respectively.

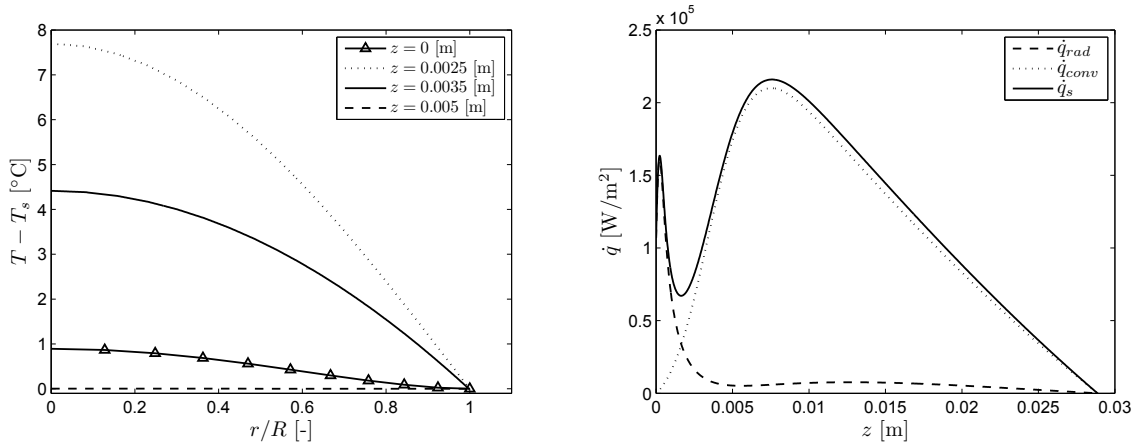

(a) (b)

Figure 4: (a) Computed normalized temperature profile $\Delta T(r,z) \equiv T(r,z) - T_s(z)$ as a function of the dimensionless radial component r/R at different z locations for experiment 2. (b) Computed radiative, convective and total surface heat fluxes along the axial component z for experiment 2.

The thermal history can be measured by the cooling rate

$$\dot{T}_c = \frac{\mathrm{D}T}{\mathrm{D}t} = v_z \frac{\partial T}{\partial z}\,, \tag{10}$$

which represents the change in temperature over time experienced by a glass particle. Because internal diffusion in the axial direction is relatively small, the cooling rate averaged over a fiber cross-section is related to the surface heat loss and radius attenuation by

$$\left\langle \dot{T}_c \right\rangle (z) \approx -\frac{2\dot{q}_s(z)}{\rho c_p R(z)}\,, \tag{11}$$

where $\langle\cdot\rangle$ represents the average over the cross-section. In order to assess the influence of the effective emissivity, two additional simulations have been performed with a constant emissivity $\epsilon = 0.35$ and $\epsilon = 0.5$, respectively. The first value corresponds to a value often found in the literature, while the second is a better approximation for the glass type considered here. The cooling rates at the fiber surface obtained with both constant emissivity values and with the effective emissivity $\epsilon(D, T)$ are compared in figure 5(a). A variation of about 10% of the maximum cooling rate is observed, where its maximum value is obtained using an effective emissivity. It is worth noting that those largest variations are observed in the convection-dominated region, although the emissivity is only related to radiation. In this case, changes in radiation lead to a different radius attenuation $R(z)$, and, through Eq. (11), to a different cooling rate. This demonstrates the tight coupling between all physical phenomena and the importance of accurate modeling.

The influence of the environment surrounding the fiber is investigated by considering different external temperatures T_{ext}. In particular, the surface cooling rates $\dot{T}_{c,s}$ for a constant temperature $T_{ext} = 650°\mathrm{C}$ (case 1), a variable external temperature with constant air properties, corresponding to $T_{ext} = 650°\mathrm{C}$ (case 2), and a variable external temperature with air properties depending on temperature (case 3) are compared. Note that in the case of a variable external temperature, $T_{ext}(z)$ is given by an exponential fit of the measured values as shown in figure 3(b). Results are summarized in figure 5(b) and show that the environment properties have a strong impact on the cooling rate. In particular, the cooling rate increases when the air temperature variation is considered since, in this case, the temperature difference $T_s - T_{ext}$, and thereby the convection, are larger. This effect is intensified when changes in air properties are taken into account. This shows that an accurate description of the external temperature is very important.

4.3 Stresses

For a Newtonian fluid, the extra-stress tensor $\boldsymbol{\tau} = 2\eta \boldsymbol{D}$ depends on the viscosity and the velocity gradients. The normal stress in the axial direction is thus defined as

$$\tau_{zz} = 2\eta(T) \frac{\partial v_z(z)}{\partial z}\,, \tag{12}$$

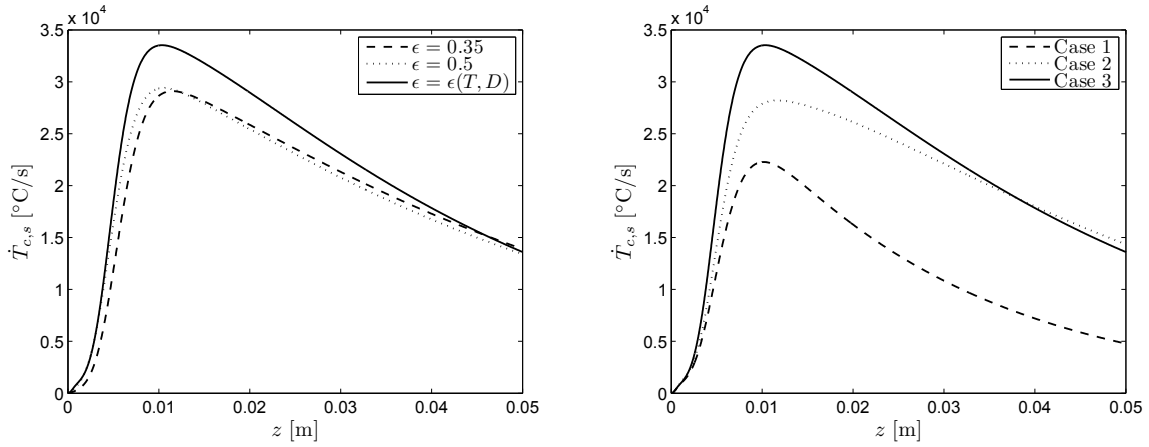

(a) (b)

Figure 5: Computed cooling rates $\dot{T}_{c,s}$ along the free surface as a function of the axial component z for experiment 2. (a) Comparison between constant emissivities and effective emissivity. (b) Comparison between a constant external temperature $T_{ext} = 650°\text{C}$ (case 1), a variable external temperature with constant air properties (case 2), and a variable temperature with air properties depending on temperature (case 3); in case 2 and 3, $T_{ext}(z)$ is given by the exponential fit of figure 3(b).

and is shown in figure 6(a). A rapid increase in τ_{zz} can be observed, which is related on the one hand to the rapid increase of the axial velocity v_z with the radius attenuation (up to four orders of magnitude), and on the other hand, to the increase in viscosity as the glass cools down ($\eta \approx 10^{12}$ Pa·s around the transition). As the fiber radius approaches its final value R_f and the glass approaches the transition temperature, the velocity gradients tend to zero but the viscosity experiences a dramatic increase, so that the final stress approaches a finite value. The normalized radial profile of the stress $\tau_{zz} - \tau_{zz,s}$ at different z locations is shown in figure 6(b). Note that in the vicinity of the tip, the axial normal stress is larger at the centerline than at the surface. The opposite is observed further away from the tip since the temperature at the surface is there lower, and thereby the viscosity much higher, than at the centerline. The stress is also sensitive to the process conditions. Figure 6(c) shows the final surface stress at the outlet, where $R = R_f$, for different final diameter values (i.e., different drawing velocities). As expected, the stress increases as the diameter is reduced (approximately as $1/D_f^2$). Additionally, as the drawing velocity increases, the velocity gradients become larger, which leads to a thinner meniscus; the cooling rate increases more rapidly, as does the viscosity. Finally, figure 6(d) shows the final surface stress for different values of the tip temperature T_0 (i.e., different volumetric flow rates) and drawing velocity such that the final diameter remains 11 μm. It can be seen that the final stress is lower when the fiberization temperature T_0 is increased.

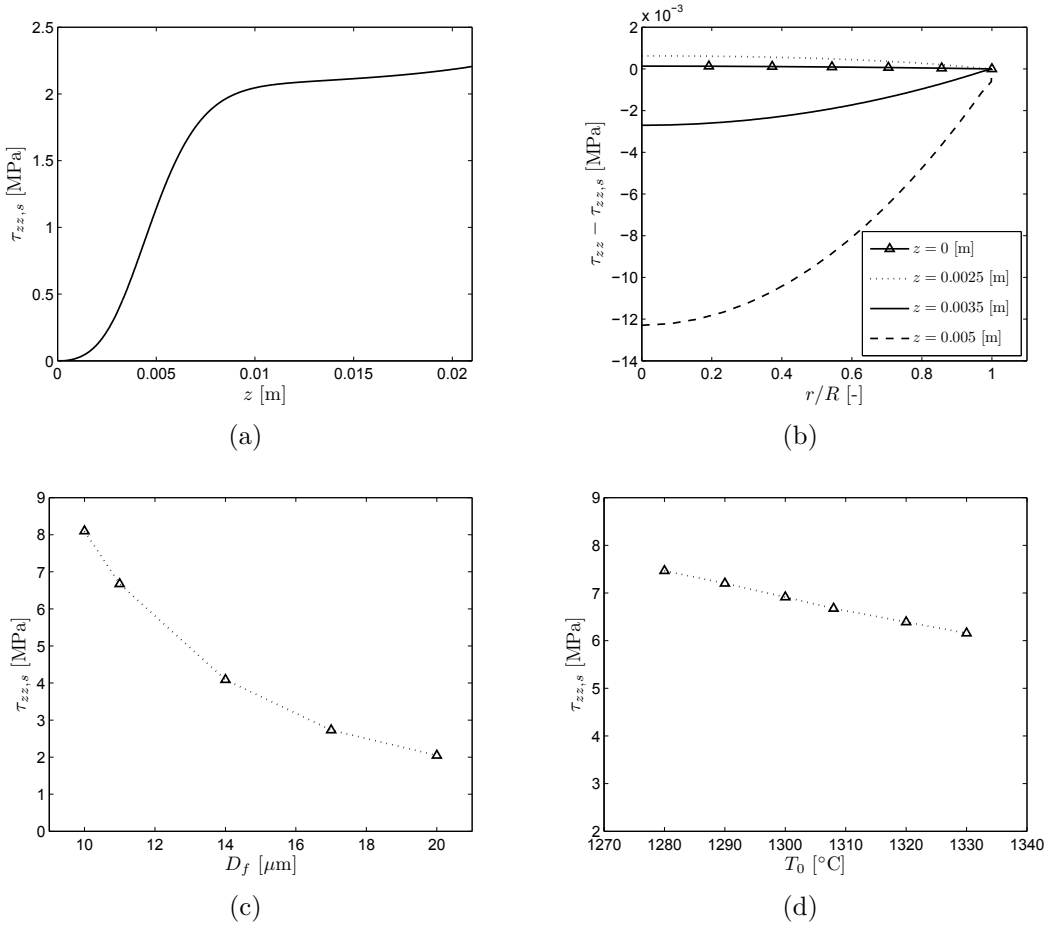

Figure 6: Computed axial normal stress τ_{zz} for experiment 2. (a) Surface stress as a function of the axial coordinate. (b) Radial profile of the normalized stress $\tau_{zz}(r, z) - \tau_{zz,s}(z)$ at different axial positions z. (c) Final surface stress as a function of the final fiber diameter (i.e., at different drawing velocities). (d) Final surface stress as a function of the tip temperature T_0 (i.e., at different flow rates).

5 Conclusion

The physics of glass fiber drawing has been investigated experimentally and numerically. The numerical results have been compared and validated with data from the literature and from a dedicated fiberization unit. Based on the numerical model, it has been demonstrated that radiation dominates in the region very close to the tip. Nonetheless, a variation of emissivity has also an impact on the fiber cooling far away from the tip, as the cooling rate depends not only on the surface heat loss but also on the attenuation of the meniscus. It was also shown that prescribing a correct external temperature is very important as the cooling rate, and thereby all other properties, are very sensitive to the

heat loss. Finally, the internal stresses have been computed and their dependence on some key parameters has been computed. Since the viscosity increases as a logarithmic law, stresses are extremely sensitive to small temperature variations. It was shown that the stresses increase when the fiber diameter and/or the fiberization temperature are reduced. In conclusion, simulations can provide a useful tool to gain insight into the physics of fiber glass drawing and to devise new strategies for adjusting the process operating window.

Future work will focus on improving the models for internal radiation and the surrounding environment, which might include numerical simulations of the air flow. The unsteady case will be considered. Additionally, the transition phase should also be included into the model. Finally, this knowledge will be used to characterize the physical mechanisms of fiber breaking.

REFERENCES

[1] Glicksman, L.R. *An investigation of the shape, temperature distribution and tension of a heated free jet flowing at ultra low reynolds number*. PhD Thesis, Massachusetts Institute of Technology (1964).

[2] Huynh, B.P. and Tanner, R.I., Study of the non-isothermal glass fibre drawing process, *Rheologica Acta* **22**, 5:482–499 (1983).

[3] Purnode, B.A. and Rubin, Y., Two-dimensional Finite Element Analysis of Glass Fiber Forming, *8th International Congress on Glass*, San Fransisco, USA (1998).

[4] Purnode, B.A., Transient Axisymmetric Study of Glass Fiber Forming, *Proceedings of ASME 2000 Fluids Engineering Division Summer Meeting*, Boston, USA (2000).

[5] Von Der Ohe, R., *Simulation of Glass Fiber Forming Processes*, Phd Thesis, Aalborg University, Denmark (2003).

[6] Rekhson, S., Leonard, J. and Sanger, P., Attenuation and Breakage in the Continuous Glass Fiber Drawing Process, *Ceram. Eng. Sci. Proc.* **25**, 1:179–190 (2004).

[7] Liu, S. and Banta, L.E., Parametric Study of Glass Fiber Drawing Process, *International Journal of Applied Glass Science* **1**, 2:180–187 (2010).

[8] Loewenstein, K.L., *The Manufacturing Technology of Continuous Glass Fibers*, Elsevier Scientific Publishing Company, New York (1973).

[9] Kase, S. and Matsuo, T.J., Studies of melt spinning I, fundamental equations on the dynamics of melt spinning, *Journal of Polymer science, Part A: General papers* **3**, 7:2541–2554 (1965).

[10] Crochet, M.J., Keunings R., Debbaut B., and Marchal J.M., Polyflow: a multipurpose finite element program for continuous polymer flows, *Computer Modeling for Extrusion and Other Continuous Polymer Processes*, 25-50 (1992).